

# JGR Space Physics



## METHOD

10.1029/2022JA030850

This article is a companion to Samsonov et al. (2022), <https://doi.org/10.1029/2022JA030848>.

### Key Points:

- Different methods of finding the location and shape of the magnetopause from X-ray images give consistent results
- Maximum integrated emissivity indicates the outer boundary of the magnetopause
- This work is made in preparation for the forthcoming Solar wind Magnetosphere Ionosphere Link Explorer mission

### Correspondence to:

A. Samsonov,  
[a.samsonov@ucl.ac.uk](mailto:a.samsonov@ucl.ac.uk)

### Citation:

Samsonov, A., Sembay, S., Read, A., Carter, J. A., Branduardi-Raymont, G., Sibeck, D., & Escoubet, P. (2022). Finding magnetopause standoff distance using a Soft X-ray Imager: 2. Methods to analyze 2-D X-ray images. *Journal of Geophysical Research: Space Physics*, 127, e2022JA030850. <https://doi.org/10.1029/2022JA030850>

Received 15 JUL 2022  
Accepted 6 DEC 2022

©2022. The Authors.

This is an open access article under the terms of the [Creative Commons Attribution License](https://creativecommons.org/licenses/by/4.0/), which permits use, distribution and reproduction in any medium, provided the original work is properly cited.

## Finding Magnetopause Standoff Distance Using a Soft X-ray Imager: 2. Methods to Analyze 2-D X-ray Images

Andrey Samsonov<sup>1</sup> , Steven Sembay<sup>2</sup> , Andrew Read<sup>2</sup>, Jennifer Alyson Carter<sup>2</sup> , Graziella Branduardi-Raymont<sup>1</sup> , David Sibeck<sup>3</sup> , and Philippe Escoubet<sup>4</sup> 

<sup>1</sup>Mullard Space Science Laboratory, University College London, Dorking, UK, <sup>2</sup>Leicester University, Leicester, UK,

<sup>3</sup>Goddard Space Flight Center NASA, Greenbelt, MD, USA, <sup>4</sup>ESA/ESTEC, Noordwijk, The Netherlands

**Abstract** The Earth's magnetosheath and cusps are the sources of soft X-rays. In the accompanying paper (Part 1) and this paper, we discuss the methods of finding the magnetopause position by analyzing the X-ray images. We use the software developed for the Soft X-ray Imager (SXI) on board the forthcoming Solar wind Magnetosphere Ionosphere Link Explorer (SMILE) mission. We show how to find the maximum SXI count rate in noisy count maps. We verify the assumption that the maximum of the X-ray emissivity integrated along the Line-of-Sight ( $I_x$ ) is tangent to the magnetopause. We consider two cases using two MHD models and apply different methods of magnetospheric masking. Overall, the magnetopause is located close to the maximum  $I_x$  gradient or between the maximum  $I_x$  gradient and the maximum  $I_x$  depending on the method used. But since the angular distance between the maximum  $I_x$  gradient and the maximum  $I_x$  is relatively small (about 3°), the maximum  $I_x$  might be used as an indicator of the outer boundary of a wide magnetopause layer usually obtained in MHD simulations.

**Plain Language Summary** This is the second of two papers presenting the techniques to estimate the Earth's magnetopause location (the outer boundary of the magnetosphere) under the impact of the highly dynamic solar wind. Our knowledge of the overall shape of the magnetopause will be vastly improved when we start using X-ray imagers to monitor large areas around this boundary as the solar wind varies. In this second paper of the series, we make use of the X-ray emissions in the vicinity of the Earth simulated in the first paper for two case studies with vastly different incoming solar wind conditions. Here we examine different methods of how to extract the magnetopause shape and position from X-ray maps of the type that will be returned by the X-ray imager due to flying on the SMILE mission.

## 1. Introduction

The Earth's magnetosheath and cusps are the sources of soft X-rays. The soft X-rays result from the Solar Wind Charge Exchange (SWCX) between heavy highly ionized solar wind ions (e.g.,  $O^{7+}$ ) and exospheric neutrals (only H for the magnetospheric emission). The heavy ion picks up an electron from the neutral, this electron enters into a high-energy orbit and then transitions to a lower-energy orbit with the emission of a photon. Recent studies (e.g., Branduardi-Raymont et al., 2012; Carter et al., 2010; Collier & Connor, 2018; Robertson et al., 2006; Sibeck et al., 2018; Sun et al., 2019; Walsh et al., 2016) showed that the X-ray emission in the magnetosheath can be measured and the two-dimensional (2-D) images obtained can be used for reconstruction of the magnetopause position and shape. A number of missions have been proposed or are being developed to implement this finding. One of these new missions, Solar wind Magnetosphere Ionosphere Link Explorer (SMILE) is due to launch in early 2025. One of the instruments onboard will be the Soft X-ray Imager (SXI) designed for measuring this X-ray emission.

In the accompanying paper (Paper 1) and this paper (Paper 2), we discuss the methods of finding the magnetopause position by analyzing the X-ray images. In Paper 1, we presented the simulations of the two MHD models, the Space Weather Modeling Framework (SWMF) and Lyon-Fedder-Mobarry (LFM), for one artificial (Case 1) and one real (Case 2) event. Since we do not expect heavy solar wind ions to penetrate into the magnetosphere, we employ the magnetospheric masking methods to outline the magnetospheric region and replace the density obtained there from the MHD simulations with zero. Note that we need the magnetospheric masking only while processing the MHD simulations and we need not use these methods for the SMILE data. We calculated the X-ray emissivity in a 3-D cube using the simulation results. All these details are presented in Paper 1. In Paper 2, we

integrate this emissivity along the line-of-sight (LOS) to obtain 2-D images. We place an imaginary spacecraft at points along the SMILE trajectory and obtain idealized integrated X-ray emissivity and SXI counts maps using software developed for SXI simulations. We show how to get the maximum emissivity by analyzing SXI counts maps including instrumental noise.

Several methods have been already suggested to analyze the X-ray images and extract the information about the three-dimensional (3-D) magnetopause, such as the tangential direction approach (Collier & Connor, 2018; Connor et al., 2021; Sun et al., 2019), the boundary fitting approach (Jorgensen, Sun, Wang, Dai, Sembay, Wei, et al., 2019; Jorgensen, Sun, Wang, Dai, Sembay, Zheng, et al., 2019), and the tangent fitting approach (Sun et al., 2020). The maximum of X-ray emissivity has been interpreted to coincide with the tangential direction to the magnetopause. The 3-D magnetopause can be reconstructed for constant solar wind conditions using a set of successive X-ray images along a spacecraft trajectory (Collier & Connor, 2018) or using only one image but making the assumption that the subsolar magnetopause is described by parametric expressions (Sun et al., 2020). However, the parametric expression in Sun et al. (2020) is not universal and, in particular, does not include the dipole tilt. In this paper, we verify the tangential direction approach using the results of MHD simulations. We discuss the accuracy of finding the magnetopause position using this approach and compare the results of different MHD models and different techniques of masking the magnetosphere in simulations.

In Paper 1, we already presented the formula for the soft X-ray emissivity  $P_x$ :

$$P_x = \alpha N_{SW} N_H V_{rel}, \quad \text{here } \alpha = 10^{-15} \text{ eV cm}^2, \quad \text{and } N_H = 25(R/10R_E)^{-3} \quad (1)$$

$P_x$  is proportional to the solar wind density  $N_{SW}$ , the exospheric neutral density  $N_H$ , and the relative velocity  $V_{rel}$ . The solar wind density and relative velocity are obtained from MHD simulations, while the neutral density varies with the geocentric distance as suggested by Cravens et al. (2001). Connor et al. (2021) compared the dayside neutral density profiles along the Sun-Earth line obtained in several publications. The different studies predict a qualitatively similar decrease in the neutral density with an increase in the radial distance, although the values near the subsolar magnetopause may be different depending on the methods applied. In particular, the neutral density at  $10 R_E$  subsolar location ranges from 4 to  $59 \text{ cm}^{-3}$  in the different models, therefore the value of  $25 \text{ cm}^{-3}$  used in our work is located somewhere in the middle between the different estimates. We expect that using other models for the neutral density would not change the conclusions of this work. Expression (1) contains the emission scale factor  $\alpha$  which depends on the charge transfer cross section, the fraction of high charge state ion species in the solar wind, the proton energy, etc. (e.g., Sibeck et al., 2018). The value of  $10^{-15} \text{ eV cm}^2$  has been used by (Jorgensen, Sun, Wang, Dai, Sembay, Wei, et al., 2019; Sun et al., 2019, 2020) and this agrees with the earlier estimations (Cravens, 2000).

We simulate two cases with a northward interplanetary magnetic field (IMF) using two global MHD models, SWMF and LFM, and apply the masking methods explained in detail in Paper 1. The first case is artificial with constant solar wind conditions that correspond to a moderately compressed magnetosphere. In the second case, we use the solar wind conditions from the Wind spacecraft on 16–17 June 2012. This event consists of an interplanetary coronal mass ejection (ICME) characterized by a large solar wind density. We do not have in situ observations of the magnetopause crossings to compare with the simulations in this case, but previous studies showed a reasonably good agreement between them in the predictions of magnetopause position (e.g., Samsonov et al., 2016).

In the next section, we briefly describe the method of finding the integrated X-ray emissivity and SXI counts maps and present the results of the simulation in cases 1 and 2. We also show how the X-ray images will change while moving along the spacecraft orbit. In Section 3, we test the hypothesis that the maximum of the integrated emissivity is located along a tangent to the magnetopause. In the last section, we discuss the results and draw conclusions.

## 2. Integrated X-ray Emissivity and SXI Counts Maps

### 2.1. SXI Simulation Software

*SXI\_SIM* is the instrument simulation software used by the SMILE SXI project. The software, written using the Interactive Data Language, is not public but is available to SXI consortium members upon request to the

project principal investigator (PI). *SXI\_SIM* outputs images and spectral data products which are predictions of the type of science data the SXI instrument will deliver for a given input. The primary input to the software is a three-dimensional data cube giving some derived prediction of the foreground SWCX X-ray emissivity  $P_x$  around the Earth and at a spacecraft/instrument position and viewing direction relative to that cube in the same coordinate system. The X-ray emissivity cube is derived from the simulations using MHD codes as described in Paper 1. The software then derives a two-dimensional map by integrating along a grid of directions within the instrument field-of-view. The units of this integrated emissivity  $I_x$  are  $\text{keV cm}^{-2} \text{s}^{-1} \text{sr}^{-1}$ .

This foreground SWCX emission map plus maps giving the predicted X-ray background in the same units for the given view direction are the primary X-ray input into the main instrument simulator. In addition, a prediction of the particle-induced background within the instrument completes the background components, however, over the main science energy band of interest (which is around 0.2–2.0 keV) the background is dominated by the direct X-ray background which is mainly comprised of astrophysical diffuse and point-like components. The project uses for this purpose published ROSAT (Truemper, 1982) data downloaded from NASA's HEASARC Data Centre (<https://heasarc.gsfc.nasa.gov>).

Finally, in addition to the input maps are spectral files giving the relative intensity of a given GSM component as a function of energy. For example, in the case of the foreground SWCX emission this is the relative strength of each charge exchange emission line as a function of energy. The SWCX spectrum is known to depend on the solar wind state (Koutroumpa et al., 2009) and for self-consistency a SWCX spectral file appropriate to the solar wind conditions used to derive the initial 3-D emissivity SWCX emissivity cube should be used.

*SXI\_SIM* then takes this input and folds the spatial maps and spectral files through the instrument response to derive a predicted total observed X-ray counts map for a given user specified integration time and output energy band. The instrument response is essentially the whole telescope effective area which is a function of energy and angular position within the field-of-view (the vignetting function). The spectral files are used to weight the output counts for the specified output energy band. The integration time and pixel size of the output maps are at the discretion of the user but are generally much larger than the native time and spatial resolution of the instrument. Poisson noise is then added at this stage to the output map.

From the total observed maps the software then finally outputs a processed version where the predicted background model is subtracted and the final background-subtracted map is corrected for the telescope vignetting function. This produces a prediction of the foreground SWCX emission but with a noise per pixel appropriate to the total input components and background subtraction process. This output ( $I_x$  and SXI counts maps) is used in the remainder of this paper.

## 2.2. Results for Case 1

We make simulations with the SWMF model and apply the masking methods explained in details in Paper 1. Case 1 is an artificial case with fixed solar wind conditions: the ion density  $N_{sw} = 12.25 \text{ cm}^{-3}$ , the velocity along Sun–Earth line 400 km/s,  $B_x = B_y = 0$ , and  $B_z = 5 \text{ nT}$ . Figure 1 shows the integrated emissivity  $I_x$  (panel a) and SXI counts maps with a  $1^\circ$  resolution for three different integration times 300, 600, and 1,200 s (panels b–d) calculated by the *SXI\_SIM* software. An imaginary spacecraft is located at  $(6.57, -5.94, 17.33) R_E$  in GSM coordinates (this corresponds to a point along the SMILE orbit near apogee in April 2025). The SXI instrument is oriented in such a way that the center of the field of view (FOV) (i.e., aim point) is directed toward the approximate subsolar magnetopause, at  $(9.7, 0, 0) R_E$ .  $\phi = 0$  on Figure 1 and below corresponds to the plane passing through the spacecraft and the  $x$  axis (Sun–Earth line). The  $\theta = 0$  plane is orthogonal to the  $\phi = 0$  plane and contains the points of the spacecraft and the aim point  $(9.7, 0, 0) R_E$ .

As expected, the source of the strongest emissivity in the FOV is the magnetosheath which has an arc-shape in Figure 1a. The integrated emissivity significantly decreases for the rays on the right side of the panel outside of the SXI FOV (for  $\theta > 8^\circ$ ), that is, for those staying completely in the supersonic solar wind. The  $I_x$  also decreases for the rays passing through the magnetosphere on the left side of panel a ( $\theta < -5^\circ$ ) but this decrease is slower than in the solar wind. Note that these rays cross both the magnetosphere and the magnetosheath on the flanks; while the magnetospheric emissivity drops to zero, the magnetosheath emissivity on the flanks is still usually higher than that in the solar wind (see, e.g., Figures 8c and 8d in Paper 1). Figures 1b–1d shows the SXI counts maps for different integration times. Ideally, we would like to observe a region of high count rates in the center

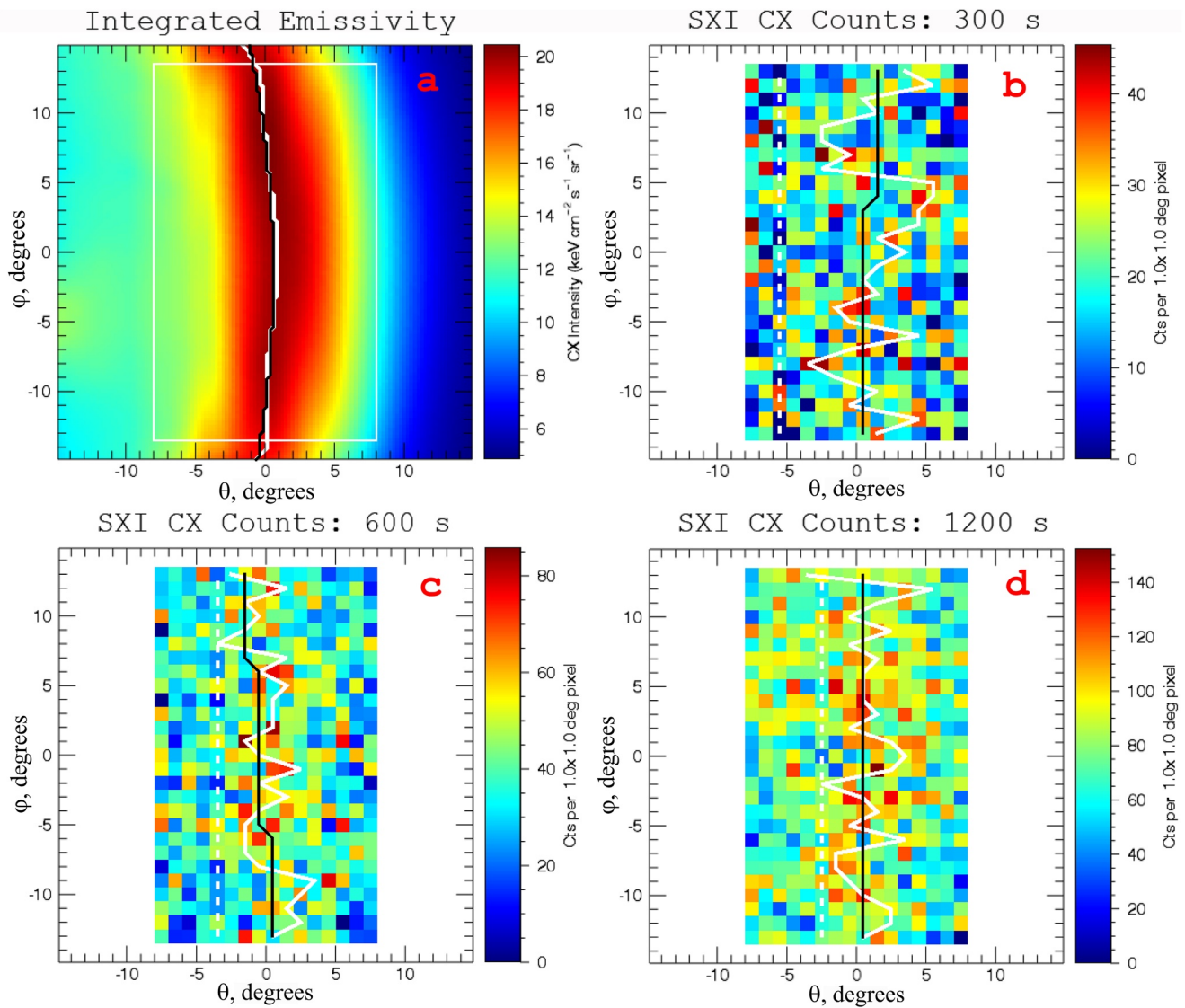


**Figure 1.** Integrated emissivity along line of sight (a) obtained from the Space Weather Modeling framework simulations in Case 1 and Soft X-ray Imager (SXI) counts maps (i.e., output of the *SXI\_SIM*) (b–d) with the exposure times of 300, 600, and 1,200 s respectively. The SXI FOV is the white rectangle in panel (a). Spacecraft position is  $(6.57, -5.94, 17.33) R_E$  (this corresponds to a point along the Solar wind Magnetosphere Ionosphere Link Explorer orbit, see Table 1), and the aim point is  $(9.7, 0, 0) R_E$  for all panels. Note that the color scale of SXI counts changes with the exposure time. Thick white lines mark the strongest emissivity or counts for each azimuth angle  $\phi$  (with the averaging over five pixels for counts maps), black lines indicate polynomial fits to the white lines, dashed white lines indicate the maximum of the average counts gradient.

of the figure with the same shape as in Figure 1a. This would be possible for a large integration time when the signal-to-noise ratio becomes large. However the calculated SXI counts maps are very noisy especially for short exposure times (300 s and even 600 s), and the maximum in counts can be hardly seen by simple visual inspection. Nevertheless, the maximum can be found by using relatively simple methods of image processing as shown below.

A general approach for finding locations of the maximum of SXI counts in a noisy picture (such as in Figures 1b–1d) is averaging and decreasing angular resolution until the location of maximum becomes visible. Our algorithm is the following. We calculate the running averages over several cells along the  $\theta$  axis for each  $\phi$  (exactly five  $1^\circ \times 1^\circ$  cells for the results in Figure 1 and later on in Figure 3) and find the location of maximum along this averaged  $\theta$ , and finally make a second order polynomial interpolation over  $\phi$ . The locations of maxima of 5-cells average and its polynomial interpolation are shown by the solid white and black lines respectively in Figures 1 and 3. Although the white lines in Figures 1b–1d have a zigzag shape because of the noise, the

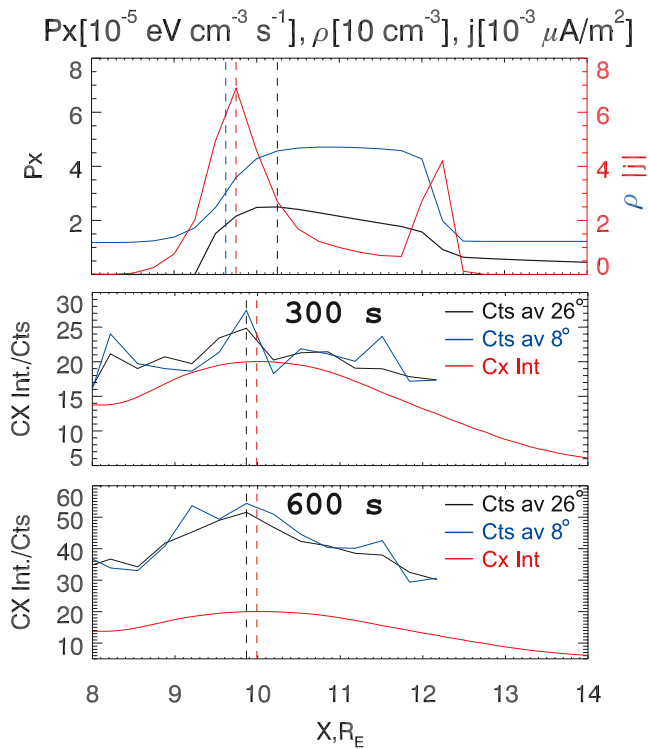


**Figure 2.** Top panel: emissivity (black), density (blue), and electric current density (red) along the Sun-Earth line; middle panel: integrated emissivity (red) in  $\text{keV cm}^{-2}\text{s}^{-1}\text{sr}^{-1}$ , Soft X-ray Imager (SXI) counts per pixel averaged over azimuthal angles  $\phi$  from  $-13$  to  $+13^\circ$  (black), SXI counts per pixel averaged over the central part ( $\phi$  from  $-4$  to  $+4^\circ$ ) (blue) for 300 s exposure time; bottom panel: in the same format as the middle panel for 600 s exposure time. Vertical lines mark maxima of  $P_x$  (black),  $j$  (red), and density gradient (blue) in the top panel, integrated emissivity (red) and SXI counts (black) in the middle and bottom panels.

$0.5 R_E$  sunward. The maxima of integrated emissivity and SXI counts are located at  $x = 9.99 R_E$  and  $x = 9.86 R_E$  respectively. The position of SXI counts maximum does not depend on the exposure time in this case. Therefore, in this particular case, the positions of the integrated emissivity (or SXI counts) maxima are  $0.2\text{--}0.4 R_E$  sunward of the magnetopause position determined from the electric current and density profiles. The position of the maximum of the integrated emissivity gradient (not highlighted) is  $x = 8.83 R_E$ , that is, nearly  $1 R_E$  earthward. With this example, we illustrate how profiles of  $\rho$ ,  $j$ , and  $P_x$  along the Sun-Earth line may appear. The location of the integrated emissivity maximum projected onto the Sun-Earth line generally does not coincide with the location of the subsolar magnetopause but can yield information about the magnetopause standoff distance under some assumptions. We discuss the methods of finding the magnetopause positions below.

### 2.3. Results for Case 2

In Case 2, an ICME with extremely high solar wind density on 16–17 June 2012 interacts with the magnetosphere. This ICME is also characterized by intervals of a large positive IMF  $B_z$  alternating with a large positive and negative IMF  $B_y$ . The auroral emission, ionospheric currents and convection in this event were studied by Carter et al. (2020).

This case demonstrates that the X-ray emissivity strongly depends on the solar wind conditions, in particular on the solar wind density and velocity. Figure 3 shows the  $I_x$  (panels a, c, e, and g) and SXI counts maps (panels b, d, f, and h) at four selected times (20:00, 22:25, and 23:10 UT on 16 June and 00:00 UT on 17 June) during the strong magnetospheric compression in this case. The exposure time for all of the SXI counts maps is 5 min. On

polynomial interpolation is smooth and passes nearly through the expected location of the maximum of emissivity in the subsolar region. We can check this if we compare the locations of the  $I_x$  maximum in Figure 1a ( $\theta \approx 1^\circ$  near the subsolar point  $\phi = 0$ ) and the polynomial fits in Figures 1b–1d. The maximum of counts rate is located at  $\theta \approx 0.5^\circ$  on panels b and d, while it is slightly shifted earthward to  $\theta \approx -0.5^\circ$  on panel c. Note that for the given distance between spacecraft and aim point, a difference in one degree corresponds to about  $0.3 R_E$  difference along the Sun-Earth line. The differences of  $0.5^\circ$  and  $1.5^\circ$  satisfy the science requirement of SMILE SXI which is  $1.5^\circ$  in a 5 min integration time (Branduardi-Raymont et al., 2018).

We find the magnetopause standoff distance at the subsolar point and compare it with the location of the  $I_x$  and SXI counts maxima. Figure 2 shows profiles of the emissivity  $P_x$ , density, and electric current density (top panel), and the integrated emissivity and SXI counts (middle and bottom panels) along the Sun-Earth line. Since both the  $I_x$  and the SXI counts depend on the angles  $\theta$  and  $\phi$ , we convert  $\theta$  to the distance along the Sun-Earth line for  $\phi = 0$ . SXI counts in the middle panel are calculated for 5 min exposure time, and those in the bottom panel for 10 min, therefore the number of SXI counts in the bottom panel is about twice that in the middle panel. The integrated emissivity (red lines) is the same in the middle and bottom panels. Vertical lines mark maxima of  $P_x$  (black),  $j$  (red), and density gradient (blue) in the top panel, integrated emissivity (red) and SXI counts (black) in the middle and bottom panels. Since the SXI counts maps are rather noisy both for 5 and 10 min exposure times, we average over the azimuthal angle  $\phi$  in the intervals  $(-4, +4)$  and  $(-13, +13)$  degrees as shown by the blue and black lines in the middle and bottom panels.

The magnetopause position can be found using either the maximum of electric current density or the maximum of density gradient. In this particular case, the two locations nearly coincide: the density gradient reaches a maximum at  $x = 9.63 R_E$  and the electric current density at  $x = 9.75 R_E$ , that is, the distance between them is one grid step (see description of the numerical models in Paper 1). The variations of the emissivity along the Sun-Earth line are smooth and its maximal point is located at  $x = 10.25 R_E$ , that is, about

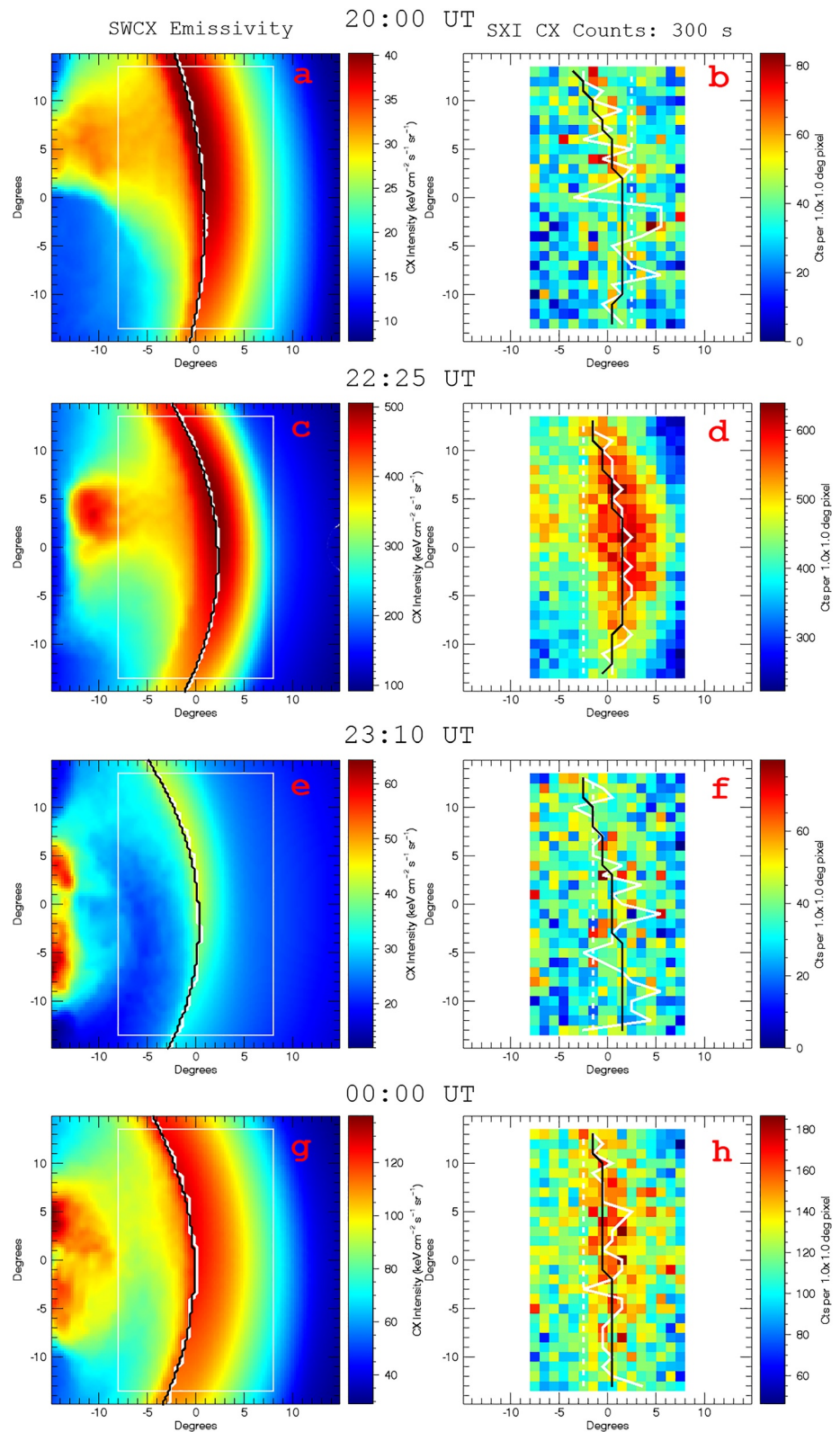


**Figure 3.** Integrated emissivity (a, c, e, and g) and Soft X-ray Imager counts maps (b, d, f, and h) with the exposure time of 5 min obtained from the Space Weather Modeling Framework simulations in Case 2. Spacecraft position is (6.57,  $-5.94$ ,  $17.33$ )  $R_E$ , and the aim point is at the subsolar magnetopause (i.e., different in each case). The solar wind densities are 14.9 (19:50 UT), 74.6 (22:15 UT), 14.7 (23:00 UT), and 39.1 (23:50 UT)  $\text{cm}^{-3}$  taking into account a 10-min time lag between the upstream boundary and subsolar magnetopause.

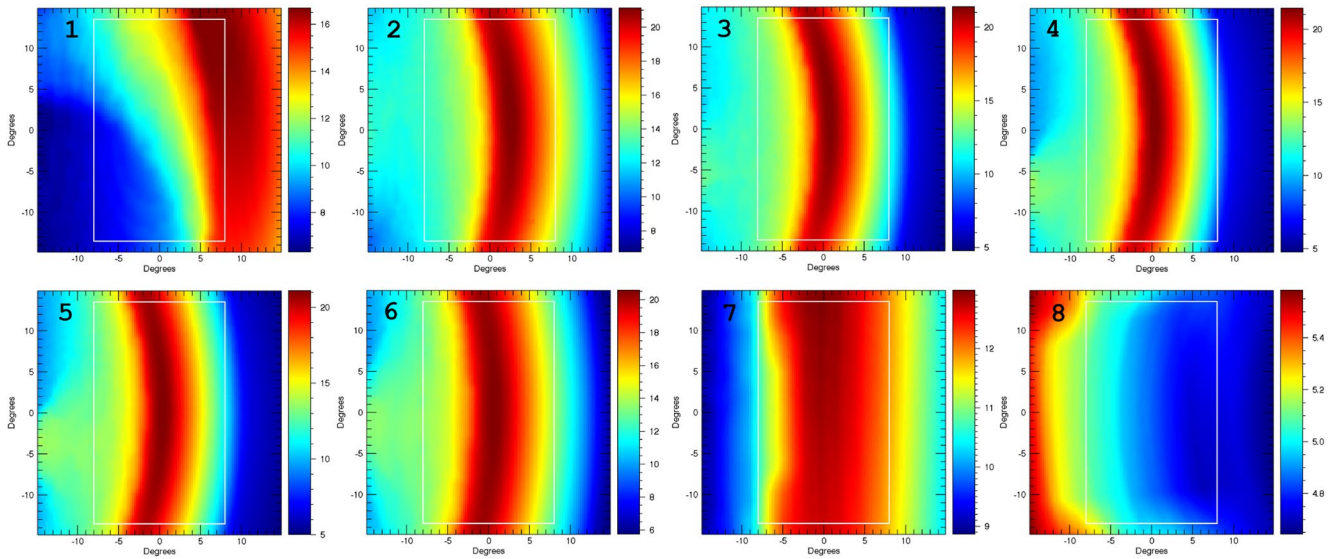


**Figure 4.** Integrated emissivity for eight points along the Solar wind Magnetosphere Ionosphere Link Explorer orbit calculated for the same MHD solution and aim point.

all panels, we can distinguish two separate regions of high  $I_x$ , the magnetosheath and cusps. The magnetosheath is a bow-shaped region passing through the center of the FOV with a perceptible maximum of  $I_x$ , and the cusps are bright spots of  $I_x$  on the left side of the images, out of the SXI FOV indicated by a white rectangle. At  $t = 22:25$  UT, the magnetospheric compression is strongest since the solar wind density reaches the maximum at that time. We obtain the maximal values of  $I_x \approx 500 \text{ keV cm}^{-2} \text{ s}^{-1} \text{ sr}^{-1}$  and of about 600 SXI counts per  $1^\circ \times 1^\circ$  pixel in the subsolar magnetosheath. The emissivity non-linearly increases with the solar wind density because the higher the solar wind density, the more compressed is the magnetosphere and, respectively, the neutral density grows up according to the expression (1).

The SWMF model predicts the minimal standoff distance of  $5.8 R_E$  at 22:25 UT, that is, well inside geosynchronous orbit. For such a strong compression, the maximum of SXI counts significantly overcomes the noise level and is easily visible on the image. On the contrary, the emissivity is weakest at 20:00 and 23:10 UT when the solar wind density is smallest during this event ( $14.9$  and  $14.7 \text{ cm}^{-3}$  respectively). At both times, the  $I_x$  maximum in the magnetosheath is about  $40 \text{ keV cm}^{-2} \text{ s}^{-1} \text{ sr}^{-1}$  and SXI counts maximum is about 60–80 counts per  $1^\circ \times 1^\circ$  pixel. The X-ray images at 20:00 and 23:10 UT look different because of the different emissivity in the cusps that determines the color scale. This distinction may result from different IMF magnitude and directions (see Table 1 and Figure 1 in Paper 1).

Using the polynomial fit (black lines) for SXI counts maps, we can reasonably well reproduce the shape of the maximal SXI counts (white zigzag lines) at 20:00 and 22:25 UT, and less successfully at 23:10 and 00:00 UT. However, we find the location of the maximum at the subsolar point with an accuracy better than  $1^\circ$  (i.e., higher than the resolution of the SXI counts maps) in all cases (compare the locations of black lines at  $\phi = 0$  on panels a and b, c and d, e and f, g, and h, respectively).

#### 2.4. Changes of X-ray Images While Moving Along the Spacecraft Orbit

Next, using Case 1 again, we illustrate how the  $I_x$  images change while a spacecraft moves along the orbit and observes the same spatial distribution of emissivity from different points of view. Figure 4 shows the  $I_x$  images and Figure 5 shows the spacecraft trajectory in the  $xz$  GSM plane where the spacecraft positions used for Figure 4 are highlighted by blue stars (the numerical sequence in Figure 4 corresponds to the clockwise direction in Figure 5). The locations match the SMILE trajectory on 9–10 April 2025. Note that the SMILE trajectory is elliptical in GSE coordinates, but becomes non-elliptical after conversion to GSM coordinates. The spacecraft moves from the nightside magnetosphere through the dayside magnetosheath and supersonic solar wind and reaches apogee near  $(x, z) = (8.3, 16.3) R_E$  (at 22:00 UT as indicated by a blue circle before the fourth star in

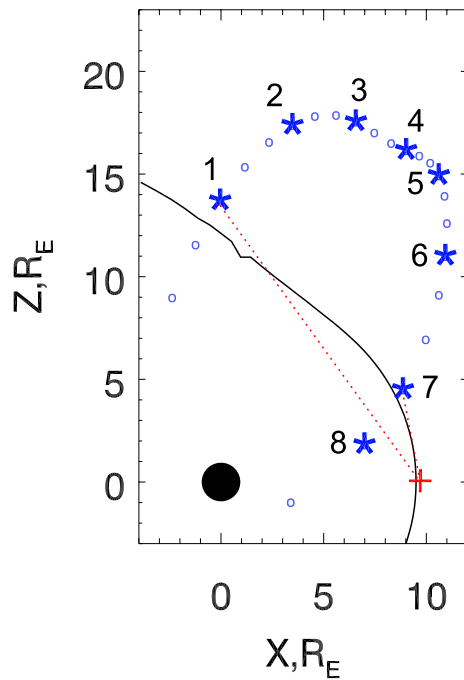


**Figure 5.** Spacecraft positions along the orbit are shown by blue circles and stars with sampling every 2 hr. The stars indicate the positions used for Figure 4. Black line marks the magnetopause defined as the open-closed field line boundary in  $y = 0$  plane. The dotted red lines show the lines of sight to the aim point from the 3rd and 21st positions along the orbit (entries 1 and 7 in Table 1).

Figure 5). When the  $z$  coordinate of the spacecraft decreases, the spacecraft moves toward the aim point at  $(9.7, 0, 0) R_E$  and crosses the magnetopause not far from the equatorial plane. Table 1 displays the eight spacecraft positions marked by blue stars in Figure 5. Note that we fix the aim point here but in reality the aim point for SMILE changes while the spacecraft moves along the orbit. If the direction to the aim point significantly differs from the tangent direction, the maximum of  $I_x$  and SXI counts will be near the edges of the FOV or even out of the FOV.

We conclude that the first and last spacecraft positions marked by stars are not suitable for SXI observations of the subsolar magnetopause because  $I_x$  maximum moves significantly away from the SXI FOV. According to Figure 5, the first point (06:00 UT 9 April) is in the magnetosheath but close to the magnetopause, near the terminator plane. Red dotted lines in Figure 5 connect the spacecraft position with the aim point near the subsolar magnetopause. Using the magnetopause position from the MHD simulation (shown by black line), we expect that most of the way between the spacecraft and aim point is located inside the magnetosphere. Since the emissivity in the magnetosphere is set equal to zero,  $I_x$  is low at the aim point and increases in the sunward direction. Even if the  $I_x$  maximum would nearly match the tangent direction as expected, the tangent point at the magnetopause is far away from the subsolar point making it difficult to find the standoff distance using the given aim point and FOV.

The last point (20:00 UT 10 April) is completely unacceptable for finding the magnetopause position because it is located inside the magnetosphere. Moreover, the radial distance to the Earth at this point is less than 50,000 km therefore the SMILE SXI would be turned off at this point. But 2 hr before, at 18:00 UT, the region of large  $I_x$  is located within the FOV as well as at other times between 12:00 UT 9 April and 18:00 UT 10 April in Figure 4, so

the location of the  $I_x$  maximum can be found. In the next section, we discuss how we can use this information for finding the magnetopause position.

### 3. Finding the Magnetopause Position in 2-D X-ray Images

#### 3.1. 2-D Images of Magnetopause Surface and Emissivity Maximum

Previous studies (e.g., Collier & Connor, 2018; Sun et al., 2020) hypothesized that the maximum of the integrated emissivity is located along a tangent to the magnetopause. We will test this hypothesis by several methods. One way to do this is to highlight all magnetospheric points in the angular coordinates  $(\theta, \phi)$  (for the given spacecraft location) and complement this image with a line that indicates the position of the maximum integrated emissivity (obtained by  $SXI\_SIM$ ). We use the polynomial fits for the corresponding  $I_x$  images (such as in Figure 1a).

Figure 6 shows the results of this method in Case 1. The grid points are interpolated to the equidistant grid with the grid step of  $0.25 R_E$ . We apply the magnetospheric masking using the thresholds conditions for the thermal pressure and velocity (Section 4.2 in Paper 1). All grid points which we determined as located in the magnetosphere are marked by small blue crosses. The outer boundary of the blue region indicates the magnetopause position. We also highlight the locations of  $I_x$  maximum (red) and of  $I_x$  maximum gradient (yellow) to see which of the two locations better matches the magnetopause position. Panels (1–4) correspond to the spacecraft positions at 12:00 and 18:00 UT on 9 April 2025 and at 00:00 and 06:00 UT on 10 April 2025 (i.e., stars 2–5 in Figure 5). We find that the position of  $I_x$  maximum gradient nearly coincides with the magnetopause position for the four spacecraft positions, and the  $I_x$  maximum is located about  $2^\circ$  sunward. We checked these results by applying the second magnetospheric masking using flowlines (Section 4.3 in Paper 1) and obtained visually the same results (not shown).

For verification of the SWMF simulations with the different magnetospheric masks, we use the LFM model which provides significant density decrease in the magnetosphere therefore the position of magnetospheric

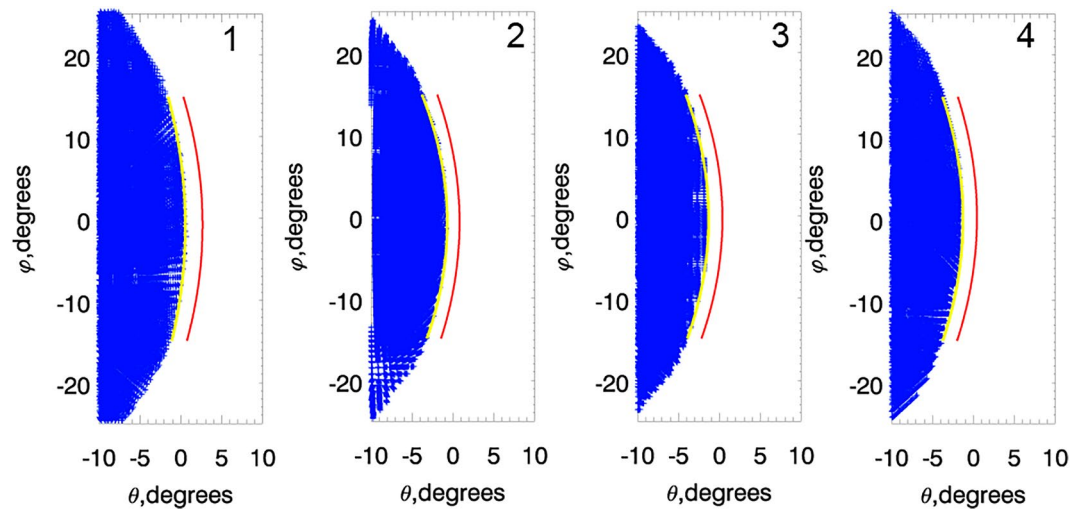


**Figure 6.** The magnetospheric points interpolated to the equidistant grid with the mask calculated by the threshold method (blue) and the locations of the maximum of  $I_x$  (red) and the maximum of  $I_x$  gradient (yellow) observed from the four spacecraft positions along the Solar wind Magnetosphere Ionosphere Link Explorer trajectory (panels 1–4 correspond to the positions at 12:00 and 18:00 UT on 9 April and at 00:00 and 06:00 UT on 10 April, see Table 1).

boundary may be found with higher accuracy. We can draw SXI images without any magnetospheric mask for this model, however we should somehow highlight magnetospheric points for the plot. Therefore we define that the grid points in the LFM simulation are located in the magnetosphere if the density is less than  $0.7 N_{SW}$  where  $N_{SW}$  is the density in the supersonic solar wind. We have checked the density thresholds at  $0.5 N_{SW}$  and  $0.9 N_{SW}$  and obtained nearly the same results. Figure 7 shows the nodes of the magnetospheric grid, the locations of the  $I_x$  maximum and of the  $I_x$  gradient maximum in the same format as in Figure 6 but for the LFM model. Again, the magnetopause location nearly coincides with the  $I_x$  gradient maximum consistent with the results of the SWMF model in Figure 6.

Alternatively, we can verify the obtained results using an analytical expression for the magnetopause. Jorgensen, Sun, Wang, Dai, Sembay, Wei, et al., (2019), Sun et al. (2020) modified the analytical function suggested by Shue et al. (1998) to describe a non-axisymmetric magnetopause. The magnetopause radial distance depends on the two angles  $\mu$  and  $\nu$ .

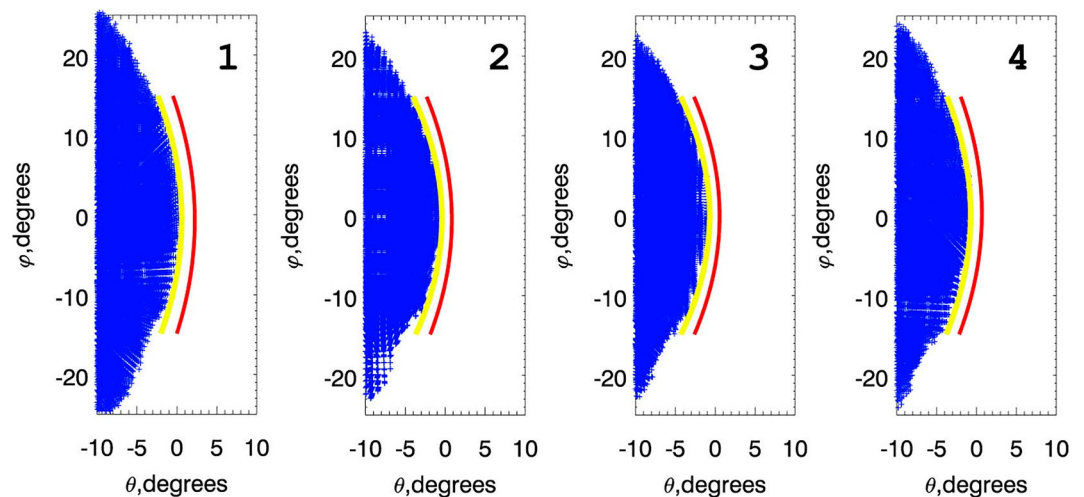


**Figure 7.** The grid points in the magnetosphere (blue), the locations of the maximum of  $I_x$  (red) and the maximum of  $I_x$  gradient (yellow) for the same spacecraft positions as in Figure 6 but for the Lyon-Fedder-Mobarry model.

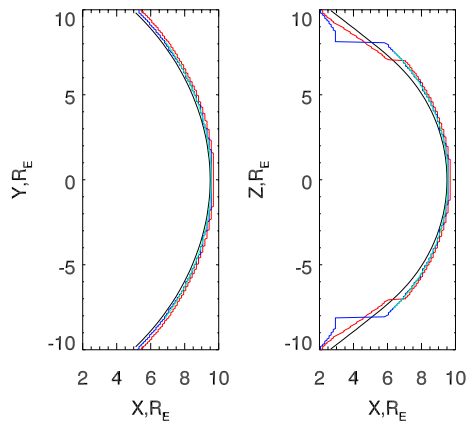


**Figure 8.** The magnetopause positions in  $xy$  (left) and  $xz$  (right) planes obtained by the locations of the open-closed field line boundary (black), of the maximum of electric current density (red), of the maximum of density gradient (blue), and that calculated by Equations 2–4 (green).

$$r(\mu, \nu) = \frac{r_y(\mu)r_z(\mu)}{\sqrt{[r_y(\mu)\sin \nu]^2 + [r_z(\mu)\cos \nu]^2}}, \quad (2)$$

$$r_y(\mu) = r_0 \left( \frac{2}{1 + \cos \mu} \right)^{\alpha_y}, \quad (3)$$

$$r_z(\mu) = r_0 \left( \frac{2}{1 + \cos \mu} \right)^{\alpha_z}. \quad (4)$$

Here,  $\mu$  is the angle between the  $\vec{r}$  (from the centre of the Earth) and  $x$  axis, and  $\nu$  is the angle between the  $y$  axis and projection of  $\vec{r}$  onto the  $yz$  plane. The three coefficients  $r_0$ ,  $\alpha_y$ , and  $\alpha_z$  define the subsolar standoff distance, and the magnetopause flaring angles on the  $xy$  and  $xz$  planes respectively. In Figure 8, we show the magnetopause positions obtained by several methods in Case 1, that is, the locations of the open-closed field line boundary (OCB), the maximum electric current density, the maximum density gradient, and, finally, the position calculated by expressions (2–4). In the last case, we find the coefficients  $r_0$ ,  $\alpha_y$ , and  $\alpha_z$  by making a best fit interpolation for the position of the maximum density gradient. Using these methods, we obtain slightly different

values of the standoff distance and the magnetopause flaring, however, the modified Shue et al.'s model shows good agreement with the boundary determined by the maximum density gradient in the  $xy$  and  $xz$  planes. This boundary is located between the OCB and the maximum electric current density, and the difference between the three boundaries near the subsolar point is less than  $0.2 R_E$ . This shows that the modified Shue et al.'s model can be used to approximate the magnetopause in the subsolar region in Case 1 with stationary solar wind conditions and without dipole tilt. We should mention, however, that the dipole tilt in real events changes the magnetopause shape and Equation 2 may become inapplicable for a tilted magnetosphere.

Below we use again the SWMF simulation in Case 1, define the magnetopause surface by Equations 2–4 as explained above, set the emissivity in the magnetosphere equal to zero, and apply the *SXI\_SIM* code. We show the magnetopause surface and the locations of the  $I_x$  maximum and of the  $I_x$  gradient maximum in Figure 9. This approach is self-consistent and slightly more accurate because we display the exact position of the magnetopause rather than highlight magnetospheric grid points. The results show that the magnetopause near the subsolar point is located between the  $I_x$  maximum and the  $I_x$  gradient maximum, but, at least for the first spacecraft positions, closer to the  $I_x$  gradient maximum. Since we highlight only the grid nodes in the magnetosphere in Figures 6 and 7 and now we draw the modeled magnetopause, the small difference between these results might be related to the grid resolution.

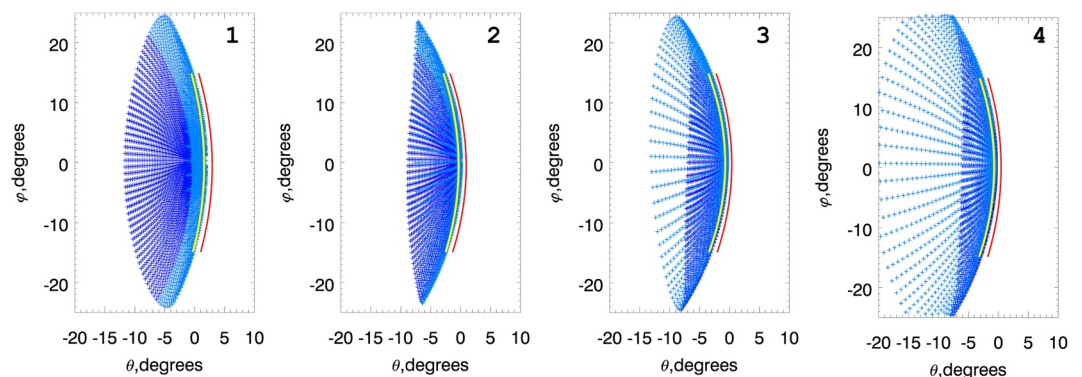


**Figure 9.** The grids on the magnetopause surface calculated by Equations 2–4 (blue), and the locations of the maximum of  $I_x$  (red) and the maximum of  $I_x$  gradient (yellow) for the same spacecraft positions as in Figure 6. Light and dark blue crosses indicate the points above and below the equatorial plane respectively.

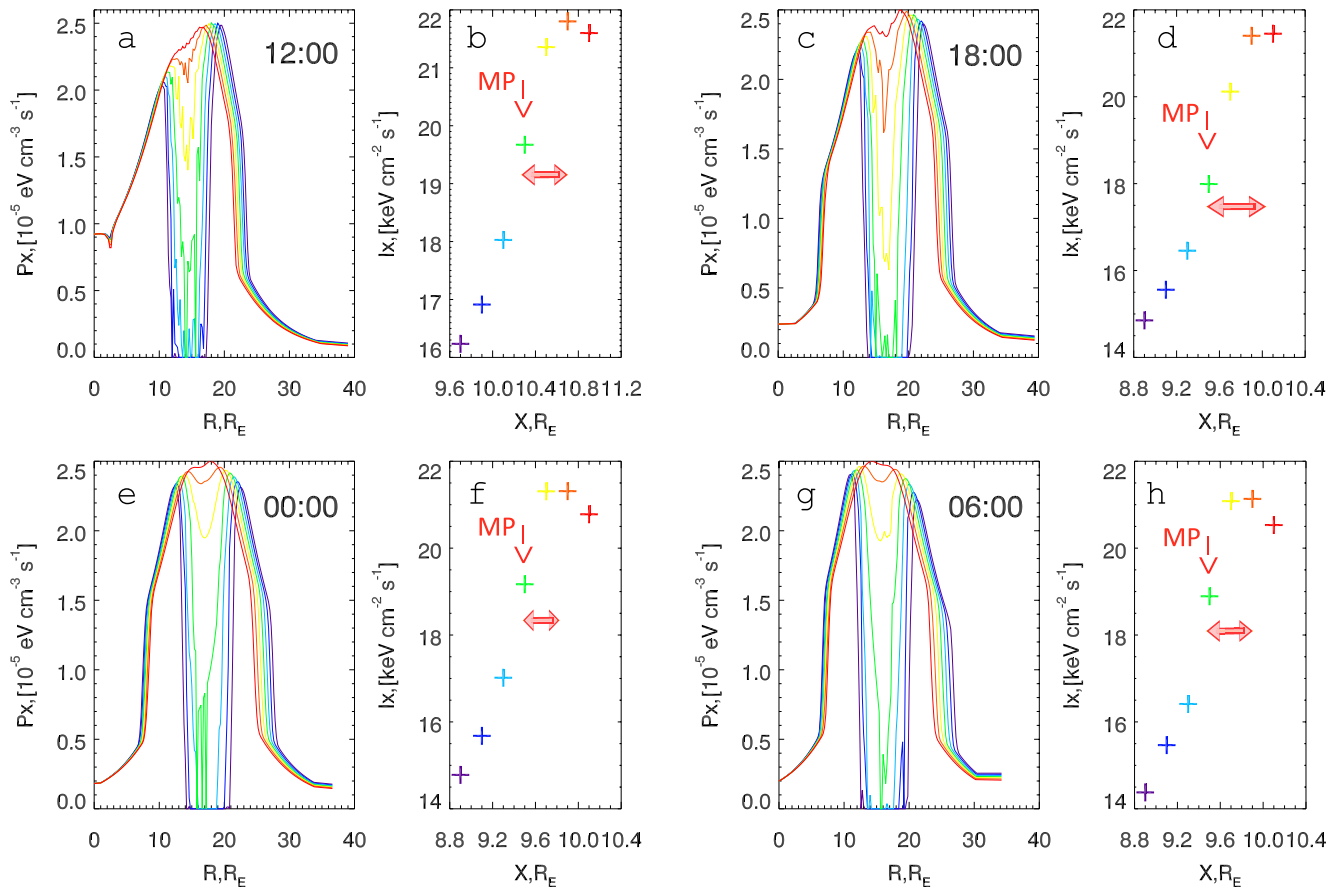


**Figure 10.** Variations of  $P_x$  along seven line-of-sight (LOSs) (with different aim points) for the four spacecraft positions at 12:00 and 18:00 UT (9 April), and 00:00 and 06:00 UT (10 April) (panels a, c, e, and g). Integrated emissivity for the same LOSs as a function of  $x$  coordinates of the aim points (i.e., intersections of the LOSs with the Sun-Earth line) (panels b, d, f, and h). Red vertical arrows indicate the supposed magnetopause position where  $P_x$  drops down to zero and the distance between the magnetopause and  $I_x$  maximum is marked by the thick horizontal arrows.

### 3.2. Emissivity Along Line-Of-Sight

We check relations between the magnetopause location and the position of  $I_x$  maximum using another approach. We use again the SWMF model and a magnetospheric mask constructed from the modified Shue et al.'s model. In Figures 10a, 10c, 10e, and 10g, we show the emissivity  $P_x$  along seven LOSs (shown by different colors on each panel) for the four spacecraft positions (the same as above, the times correspond to those in Table 1). The lines go from the spacecraft position ( $R = 0$ ) through the points distributed along the Sun-Earth line and separated by  $0.2 R_E$  (we also used the distance of  $0.1 R_E$  for panels c and d and found that the difference is small [not shown]). The emissivity is low in the solar wind (the spacecraft position near apogee is located in the solar wind), it grows up at the bow shock and through the magnetosheath, then if the line crosses the magnetopause the emissivity drops down to zero and grows up again on the outward magnetopause crossing. If the line does not cross the magnetopause, no drop in the middle occurs. Figures 10b, 10d, 10f, and 10h displays the integrated emissivity  $I_x$  for the same LOSs. On these panels, the horizontal axis is the  $x$  coordinate of the aim points at the Sun-Earth line. For finding the emissivity at each point along the LOS, we use linear interpolation between the nearest grid points. However, if the nearest grid point is located in the magnetosphere (where  $P_x = 0$ ), the emissivity at this point along the LOS is also set to equal zero. Considering the magnetopause as a discontinuity, the magnetopause is located exactly at the points where  $P_x$  drops to zero.

On all panels, the green line is the outermost LOS that crosses the magnetopause because the lines more distant from the Earth do not drop to zero. We indicate the supposed magnetopause position in panels b, d, f, and h with red arrows. The distance along the Sun-Earth line between the expected magnetopause and the maximum of  $I_x$  is about  $0.4 R_E$  (smallest in panel f and largest in panel d). If we recalculate this in terms of angles, this corresponds

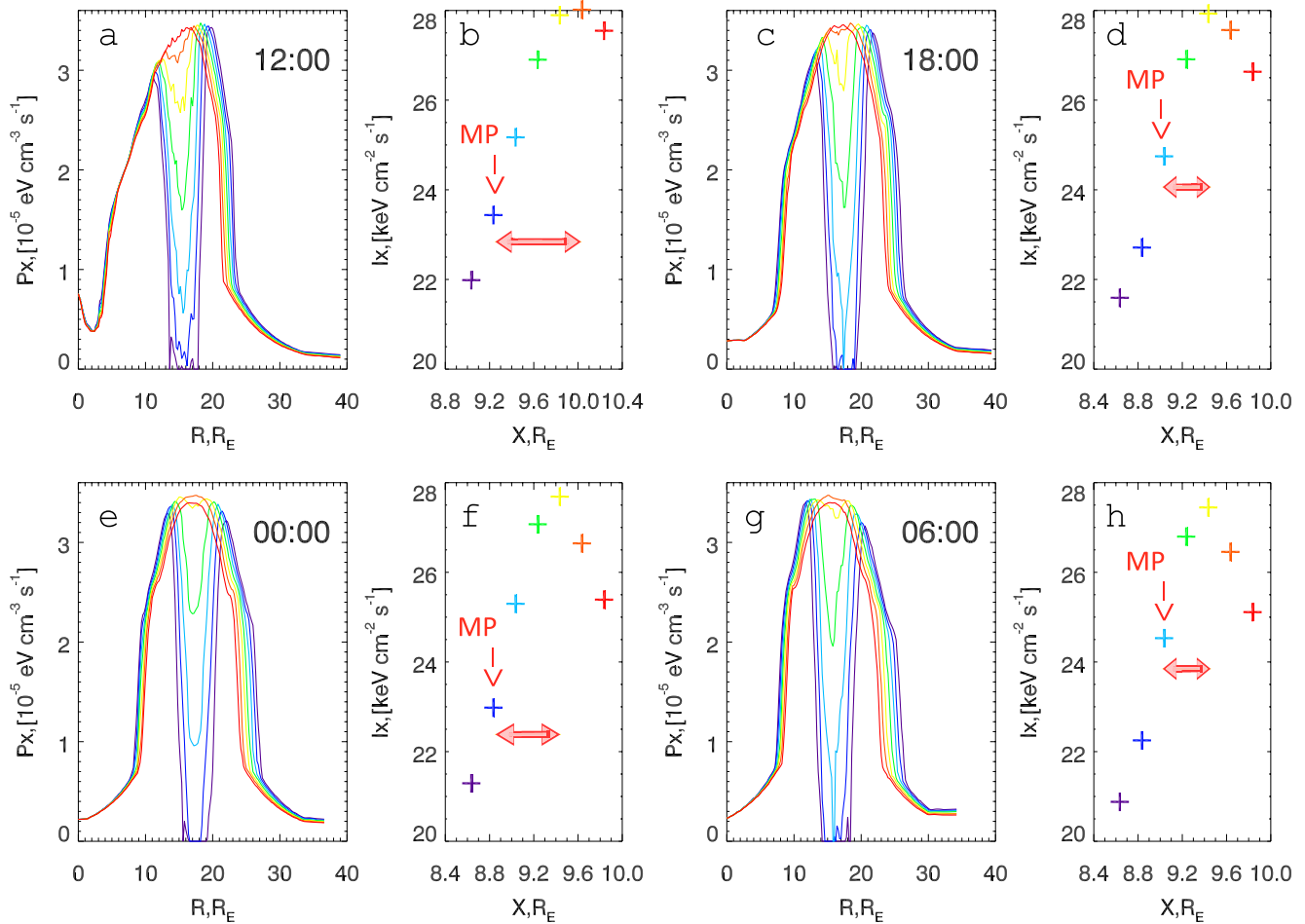


**Figure 11.** Variations of  $P_x$  along line-of-sights (a, c, e, g) and integrated emissivity (b, d, f, h) in the same format as in Figure 10 but for the Lyon-Fedder-Mobarry model.

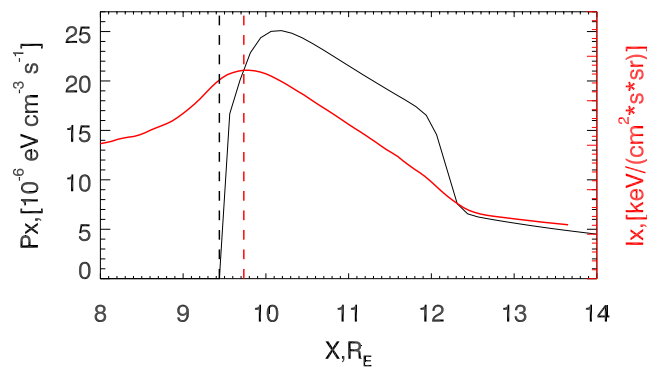
to  $1.2\text{--}1.5^\circ$  difference. Considering the slope of  $I_x$  (in panels b, d, f, h), we could conclude that the tangent LOSs roughly correspond to the maximum  $I_x$  gradient in agreement with the previous results in this section. Overall, this method is not very accurate since we determine the magnetopause position with a step along the Sun-Earth line of  $0.2 R_E$ .

Figure 11 shows similar results for the LFM model. The dark blue lines in panels a and e, and the light blue lines in panels c and g are the outermost LOSs that cross the magnetopause. The  $I_x$  maximum is located near the orange cross in panel b and near the yellow cross in panels d, f, and h. The difference between the magnetopause position and  $I_x$  maximum varies between  $0.4$  and  $0.8 R_E$ , that is, often larger than that in Figure 10. And again the magnetopause is located near the maximum  $I_x$  gradient.

### 3.3. Profiles Along the Sun-Earth Line

If the differences between the spacecraft  $x$  and  $y$  coordinates and the corresponding coordinates of the subsolar (and aim) point are much smaller than the spacecraft  $z$ , the tangent line touches the magnetopause near the subsolar point. In this particular case, we can compare the emissivity profiles along the Sun-Earth line with the  $I_x$  after conversion of the angles  $\theta$  to the distances along  $x$ . Figure 12 compares the  $P_x$  and  $I_x$  profiles calculated for the spacecraft position at 06:00 UT on 10 April ( $10.6, -3.2, 14.7 R_E$ ).

The emissivity drops to zero at  $x = 9.4 R_E$  which indicates the magnetopause location, and the  $I_x$  maximum is located at  $x = 9.7 R_E$ . Considering the magnetopause as a thin boundary, this boundary is located roughly in the middle between the  $I_x$  maximum and the  $I_x$  gradient maximum (at about  $9.2 R_E$ ). However, we note that the



**Figure 12.** Profiles  $P_x$  (black) and  $I_x$  (red) along the Sun-Earth line. For the  $I_x$  profile, we convert angle  $\theta$  to distance along  $x$  for the spacecraft position at 06:00 UT on 10 April. Vertical lines indicate the drop of  $P_x$  to zero (black) and the  $I_x$  maximum (red).

magnetopause in MHD simulations is a layer with a typical thickness equal to several grid spacings. In Figure 12, the decrease in  $P_x$  toward the magnetopause begins at  $x = 10.2 R_E$ . This does not mean that the outer boundary of the magnetopause is there. This is a northward IMF case therefore the plasma depletion layer (PDL) (e.g., Zwan & Wolf, 1976, see more references in Discussion) also occurs upstream of the magnetopause. However, we can reasonably suggest that the outer boundary of the thick magnetopause layer (obtained in the simulations) may nearly coincide with the maximum of  $I_x$ . We draw a similar plot for the spacecraft position at 00:00 UT and obtain nearly the same results.

### 3.4. 2-D Images of Magnetopause Surface in Case 2

We use the same methods to verify the tangent direction assumption in Case 2 at 20:00 UT on 16 June 2012. The spacecraft position matches that at 20:00 UT on 9 April 2025 in Table 1. In Figure 13, we show the magnetospheric points, the maximum emissivity, and the maximum emissivity gradient in the same format as in Figures 6 and 7. Panel a and b display the results of the SWMF and LFM models respectively.

The results in Case 2 closely match the results in Case 1 for both numerical models (see Figures 6 and 7). The outer boundary of the magnetospheric region, that is, the magnetopause, nearly coincides with the position of the  $I_x$  gradient maximum in the subsolar region for both models. However, contrary to Case 1, the positions of the maximum  $I_x$  and maximum  $\text{grad}(I_x)$  are asymmetric, in such a way that the magnetopause slightly shifts toward the  $I_x$  maximum on the dusk flank. The reason for the asymmetry is probably related to a strong dipole tilt in Case 2.

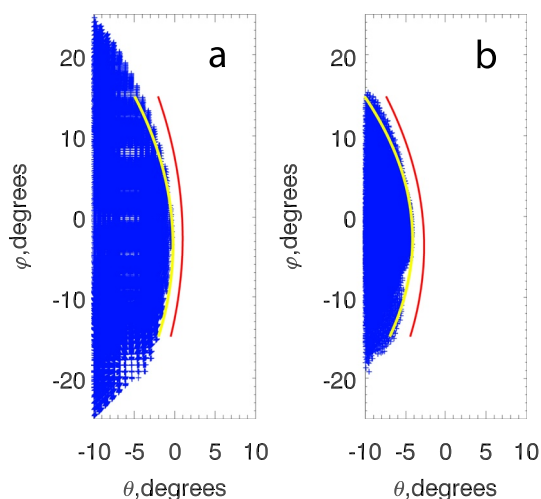


**Figure 13.** The magnetospheric points (blue), the maximum emissivity (red), and the maximum emissivity gradient (yellow) in the Space Weather Modeling Framework model (a) and in the Lyon-Fedder-Mobarry model (b) in Case 2.

## 4. Discussion and Conclusions

The two companion papers (Paper 1 and 2) present a new method of finding the magnetopause standoff distance using simulated soft X-ray images. In Paper 1, we present the MHD simulations and discuss the methods of magnetospheric masking for outlining the magnetospheric region in the simulations. These MHD results provide the necessary input conditions for the simulations in this paper. Here, we introduce the numerical code *SXI\_SIM* which simulates the output of the SXI on board the forthcoming SMILE mission. We display a set of images in the two cases, artificial and real, and for the two MHD models, SWMF and LFM. Using *SXI\_SIM*, we obtain the integrated emissivity for the given spacecraft position and the FOV, and the SXI counts maps which take into account the instrument response and include background noise. We discuss how we can find the location of the maximum of the  $I_x$  and SXI counts from these images by making a polynomial fit. Although the SXI counts maps look very noisy, the position of the maximum

**Table 1**

*Solar Wind Magnetosphere Ionosphere Link Explorer Positions in GSM Coordinates in 2025, the Same Positions Used for Simulations of  $I_x$  Images in Figure 4 and Marked by Stars in Figure 5*

|                 |                  |                  |                 |                 |
|-----------------|------------------|------------------|-----------------|-----------------|
| UT, Date        | 06:00 9 April    | 12:00 9 April    | 18:00 9 April   | 00:00 10 April  |
| Position, $R_E$ | -0.0, -3.7, 13.5 | 3.5, -2.3, 17.1  | 6.6, -5.9, 17.3 | 9.0, -7.3, 15.9 |
| UT, Date        | 06:00 10 April   | 12:00 10 April   | 18:00 10 April  | 20:00 10 April  |
| Position, $R_E$ | 10.6, -3.2, 14.7 | 10.9, -0.9, 10.8 | 8.9, -1.0, 4.3  | 7.0, -0.2, 1.6  |

counts can be accurately found in all studied cases. Alternatively, we can average the SXI counts over azimuthal angle  $\phi$  and also obtain a well-defined maximum of counts too. We display how the SXI images change when SMILE moves along its elliptical orbit.

In Section 3, we verify the assumption that the maximum of the integrated emissivity is located along a tangent to the magnetopause using several methods. In the first method, we draw images that display the locations of all simulation grid points in the magnetosphere superimposed by the locations of the maximum integrated emissivity, and the maximum gradient of integrated emissivity. The outer boundary of the magnetospheric domain is by definition the magnetopause. We find that the magnetopause is located near the maximum  $I_x$  gradient in the subsolar region for both models independent of the spacecraft position (see Figures 6 and 7). However, if we apply a slightly different approach and draw the magnetopause surface using the modified Shue et al.'s model expressed by Equations 2–4, we obtain that the magnetopause is located between the maximum  $I_x$  gradient and maximum  $I_x$  (Figure 9). The difference is relatively small and might be explained by numerical grid resolution.

In the second method, we draw the emissivity profiles along several lines of sight passing near the subsolar point. The emissivity drops to zero if the line crosses the magnetopause, therefore, we can find which of the lines is the outermost that crosses the magnetopause. This line is nearly tangent to the magnetopause. Then we calculate the integrated emissivity along the same LOSs and find their maximum location. In this method, the maximum  $I_x$  gradient better represents the magnetopause, but we realize that the accuracy of this approach is limited again by spatial resolution. In the third method, we compare the profile of emissivity along the Sun-Earth line with the profile of integrated emissivity calculated also in terms of the distance along the Sun-Earth line while the spacecraft is located nearly vertically above the subsolar point (i.e., the differences in  $x$  and  $y$  coordinates between the spacecraft and subsolar point are smaller than in  $z$ ). Here, we obtain that the magnetopause is located between the maximum  $I_x$  gradient and the maximum  $I_x$ . The distance between the magnetopause ( $P_x = 0$ ) and the  $I_x$  maximum is  $0.3 R_E$  in the considered case.

We briefly summarize the above paragraphs as follows. We find that the magnetopause is located near the  $I_x$  gradient maximum in the method with highlighted magnetospheric points (Figures 6, 7, and 13) and in the method with  $P_x$  profiles along LOSs (Figures 10 and 11). The magnetopause is located between the  $I_x$  gradient maximum and the  $I_x$  maximum in the method with interpolated magnetopause (by Shue et al.'s model) (Figure 9) and in the method with profiles along the Sun-Earth line (Figure 12). The differences in the results of the methods, however, are relatively small ( $0.2$ – $0.3 R_E$  along the Sun-Earth line) and might be explained by the uncertainty of the magnetopause positioning on a spatial scale of the grid step.

The position of the maximum  $I_x$  depends also on the density and velocity distribution in the magnetosheath. In particular, the PDL occurs in the magnetosheath close to the magnetopause. The PDL was predicted numerically by (Lees, 1964) and (Zwan & Wolf, 1976), observed by (Crooker et al., 1979), and its appearance depending on the solar wind conditions was studied by (e.g., Farrugia et al., 1997; Pudovkin et al., 1982, 1995; Samsonov, 2006; Samsonov & Hubert, 2004; Siscoe et al., 2002; Slivka et al., 2015; Y. L. Wang et al., 2003; Y. Wang et al., 2004). The magnetosheath velocity also depends on the solar wind conditions but it is probably less variable than the density. Respectively, the maximum density in the magnetosheath is often separated from the magnetopause by the PDL, and the PDL width depends on the solar wind conditions. Consequently, the distribution of the X-ray emissivity in the magnetosheath may significantly change (e.g., see  $P_x$  profiles along the Sun-Earth line at different times in Figure 12 of Paper 1). We think that it may be difficult to find a universal solution that defines the location of the tangent to magnetopause with respect to the observed maximum  $I_x$  and maximum  $\text{grad}(I_x)$ .

Both cases in this paper are characterized by a strong northward IMF and moderate or strong solar wind density. Summarizing our results, we conclude that the tangent to the magnetopause is generally located between the maximum  $I_x$  gradient and the maximum  $I_x$ , but probably closer to the maximum  $I_x$  gradient. By considering more events with different solar wind conditions and using better spatial resolution in simulations in future studies, we will get more accurate estimates of the standoff distance and develop more comprehensive methods of the magnetopause finding.

## Data Availability Statement

This work was carried out using the SWMF/BATSRUS tools developed at The University of Michigan Center for Space Environment Modeling and the LFM-MIX model available through the NASA Community Coordinated Modeling Center (<http://ccmc.gsfc.nasa.gov>). In particular, we used results of the runs *Andrei\_Samsonov\_080818\_2*, *Andrei\_Samsonov\_083118\_1*, *Andrei\_Samsonov\_021819\_1*, *Andrey\_Samsonov\_070519\_1*, and *Andrey\_Samsonov\_073119\_1*.

## Acknowledgments

AAS and GBR acknowledge support from the UK Space Agency under grant ST/T002964/1. AAS work is also partly supported by the International Space Science Institute (ISSI). JAC is supported by the Royal Society Dorothy Hodgkin Fellowship.

## References

- Branduardi-Raymont, G., Sembay, S. F., Eastwood, J. P., Sibeck, D. G., Abbey, T. A., Brown, P., et al. (2012). Axiom: Advanced x-ray imaging of the magnetosphere. *Experimental Astronomy*, 33(2–3), 403–443. <https://doi.org/10.1007/s10686-011-9239-0>
- Branduardi-Raymont, G., Wang, C., & Escoubet, C. P. (2018). *Smile definition study report (No. 1)*. European Space Agency. ESA/SCI. Retrieved from <https://sci.esa.int/web/smile/-/61194-smile-definition-study-report-red-book>
- Carter, J. A., Milan, S. E., Fogg, A. R., Sangha, H., Lester, M., Paxton, L. J., & Anderson, B. J. (2020). The evolution of long-duration cusp spot emission during lobe reconnection with respect to field-aligned currents. *Journal of Geophysical Research: Space Physics*, 125(7), e2020JA027922. <https://doi.org/10.1029/2020JA027922>
- Carter, J. A., Sembay, S., & Read, A. M. (2010). A high charge state coronal mass ejection seen through solar wind charge exchange emission as detected by XMM-Newton. *Monthly Notices of the Royal Astronomical Society*, 402(2), 867–878. <https://doi.org/10.1111/j.1365-2966.2009.15985.x>
- Collier, M. R., & Connor, H. K. (2018). Magnetopause surface reconstruction from tangent vector observations. *Journal of Geophysical Research: Space Physics*, 123(12), 10189–10199. <https://doi.org/10.1029/2018JA025763>
- Connor, H. K., Sibeck, D. G., Collier, M. R., Baliukin, I. I., Branduardi-Raymont, G., Brandt, P. C., et al. (2021). Soft X-ray and ENA imaging of the Earth's dayside magnetosphere. *Journal of Geophysical Research: Space Physics*, 126(3), e2020JA028816. <https://doi.org/10.1029/2020JA028816>
- Cravens, T. E. (2000). Heliospheric X-ray emission associated with charge transfer of the solar wind with interstellar neutrals. *The Astrophysical Journal*, 532(2), L153–L156. <https://doi.org/10.1086/312574>
- Cravens, T. E., Robertson, I. P., & Snowden, S. L. (2001). Temporal variations of geocoronal and heliospheric X-ray emission associated with the solar wind interaction with neutrals. *Journal of Geophysical Research*, 106(A11), 24883–24892. <https://doi.org/10.1029/2000JA000461>
- Crooker, N. U., Eastman, T. E., & Stiles, G. S. (1979). Observations of plasma depletion in the magnetosheath at the dayside magnetopause. *Journal of Geophysical Research*, 84(A3), 869–874. <https://doi.org/10.1029/JA084iA03p00869>
- Farrugia, C. J., Erkaev, N. V., Biernat, H. K., Lawrence, G. R., & Elphic, R. C. (1997). Plasma depletion layer model for low Alfvén Mach Number: Comparison with ISEE observations. *Journal of Geophysical Research*, 102(A6), 11315–11324. <https://doi.org/10.1029/97JA00410>
- Jorgensen, A. M., Sun, T., Wang, C., Dai, L., Sembay, S., Wei, F., et al. (2019). Boundary detection in three dimensions with application to the SMILE mission: The effect of photon noise. *Journal of Geophysical Research: Space Physics*, 124(6), 4365–4383. <https://doi.org/10.1029/2018JA025919>
- Jorgensen, A. M., Sun, T., Wang, C., Dai, L., Sembay, S., Zheng, J., & Yu, X. (2019). Boundary detection in three dimensions with application to the smile mission: The effect of model-fitting noise. *Journal of Geophysical Research: Space Physics*, 124(6), 4341–4355. <https://doi.org/10.1029/2018JA026124>
- Koutroumpa, D., Lallement, R., Raymond, J. C., & Kharchenko, V. (2009). The solar wind charge-transfer X-ray emission in the 1/4 keV energy range: Inferences on local Bubble hot gas at low  $Z$ . *The Astrophysical Journal*, 696(2), 1517–1525. <https://doi.org/10.1088/0004-637X/696/2/1517>
- Lees, L. (1964). Interaction between the solar plasma wind and the geomagnetic cavity. *AIAA Journal*, 2(9), 1576–1582. <https://doi.org/10.2514/3.2622>
- Pudovkin, M. I., Heyn, M. F., & Lebedeva, V. V. (1982). Magnetosheath's parameters and their dependence on intensity and direction of the solar wind magnetic field. *Journal of Geophysical Research*, 87(A10), 8131–8138. <https://doi.org/10.1029/JA087iA10p08131>
- Pudovkin, M. I., Zaitseva, S. A., & Besser, B. P. (1995). Magnetopause magnetic barrier parameters in dependence on the solar wind magnetic field orientation. *Annales Geophysicae*, 13(8), 828–835. <https://doi.org/10.1007/s00585-995-0828-y>
- Robertson, I. P., Collier, M. R., Cravens, T. E., & Fok, M.-C. (2006). X-ray emission from the terrestrial magnetosheath including the cusps. *Journal of Geophysical Research*, 111(A12), A12105. <https://doi.org/10.1029/2006JA011672>
- Samsonov, A. (2006). Numerical modelling of the Earth's magnetosheath for different IMF orientations. *Advances in Space Research*, 38(8), 1652–1656. <https://doi.org/10.1016/j.asr.2005.06.009>
- Samsonov, A., Carter, J. A., Read, A., Sembay, S., Branduardi-Raymont, G., Sibeck, D., & Escoubet, P. (2022). Finding magnetopause standoff distance using a soft X-ray imager: 1. Magnetospheric masking. *Journal of Geophysical Research: Space Physics*, 127, e2022JA030848. <https://doi.org/10.1029/2022JA030848>
- Samsonov, A. A., Gordeev, E., Tsyganenko, N. A., Šafránková, J., Němeček, Z., Šimunek, J., et al. (2016). Do we know the actual magnetopause position for typical solar wind conditions? *Journal of Geophysical Research*, 121(7), 6493–6508. <https://doi.org/10.1002/2016JA022471>
- Samsonov, A. A., & Hubert, D. (2004). Steady state slow shock inside the earth's magnetosheath: To be or not to be? 2. Numerical three-dimensional MHD modeling. *Journal of Geophysical Research*, 109(A1), A01218. <https://doi.org/10.1029/2003JA010006>
- Shue, J.-H., Song, P., Russell, C. T., Steinberg, J. T., Chao, J. K., Zastenker, G., et al. (1998). Magnetopause location under extreme solar wind conditions. *Journal of Geophysical Research*, 103(A8), 17691–17700. <https://doi.org/10.1029/98JA01103>

- Sibeck, D. G., Allen, R., Aryan, H., Bodewits, D., Brandt, P., Branduardi-Raymont, G., et al. (2018). Imaging plasma density structures in the soft X-rays generated by solar wind charge exchange with neutrals. *Space Science Reviews*, 214(4), 79. <https://doi.org/10.1007/s11214-018-0504-7>
- Siscoe, G. L., Crooker, N. U., Erickson, G. M., Sonnerup, B. U. Ö., Maynard, N. C., Schoendorf, J. A., et al. (2002). MHD properties of magnetosheath flow. *Planetary and Space Science*, 50(5–6), 461–471. [https://doi.org/10.1016/S0032-0633\(02\)00026-0](https://doi.org/10.1016/S0032-0633(02)00026-0)
- Slivka, K. Y., Semenov, V. S., Erkaev, N. V., Dmitrieva, N. P., Kubyshekin, I. V., & Lammer, H. (2015). Peculiarities of magnetic barrier formation for southward and northward directions of the IMF. *Journal of Geophysical Research: Space Physics*, 120(11), 9471–9483. <https://doi.org/10.1002/2015JA021250>
- Sun, T. R., Wang, C., Connor, H. K., Jorgensen, A. M., & Sembay, S. (2020). Deriving the magnetopause position from the soft X-ray image by using the tangent fitting approach. *Journal of Geophysical Research: Space Physics*, 125(9), e2020JA028169. <https://doi.org/10.1029/2020JA028169>
- Sun, T. R., Wang, C., Sembay, S. F., Lopez, R. E., Escoubet, C. P., Branduardi-Raymont, G., et al. (2019). Soft x-ray imaging of the magnetosheath and cusps under different solar wind conditions: MHD simulations. *Journal of Geophysical Research: Space Physics*, 124(4), 2435–2450. <https://doi.org/10.1029/2018JA026093>
- Truemper, J. (1982). The ROSAT mission. *Advances in Space Research*, 2(4), 241–249. [https://doi.org/10.1016/0273-1177\(82\)90070-9](https://doi.org/10.1016/0273-1177(82)90070-9)
- Walsh, B. M., Collier, M. R., Kuntz, K. D., Porter, F. S., Sibeck, D. G., Snowden, S. L., et al. (2016). Wide field-of-view soft X-ray imaging for solar wind-magnetosphere interactions. *Journal of Geophysical Research: Space Physics*, 121(4), 3353–3361. <https://doi.org/10.1002/2016JA022348>
- Wang, Y., Raeder, J., & Russell, C. (2004). Plasma depletion layer: Magnetosheath flow structure and forces. *Annals of Geophysics*, 22(3), 1001–1017. <https://doi.org/10.5194/angeo-22-1001-2004>
- Wang, Y. L., Raeder, J., Russell, C. T., Phan, T. D., & Manapat, M. (2003). Plasma depletion layer: Event studies with a global model. *Journal of Geophysical Research*, 108(A1), 1010. SMP 8-1-SMP 8-15. <https://doi.org/10.1029/2002JA009281>
- Zwan, B. J., & Wolf, R. A. (1976). Depletion of solar wind plasma near a planetary boundary. *Journal of Geophysical Research*, 81(10), 1636–1648. <https://doi.org/10.1029/JA081i1010p01636>